7

Recent Advances in Electrocatalysts for Hydrogen Oxidation Reaction in Alkaline Electrolytes

Indra N. Pulidindi[1] *and Meital Shviro*[2]

[1] *GSFC University, School of Science, Vigyan Bhavan, Fertilizernagar, Vadodara 391750, India*
[2] *National Renewable Energy Laboratory (NREL), Chemistry and Nanoscience Center, 15013 Denver West Parkway, Golden, CO 80401, USA*

7.1 Introduction

Anion-exchange membrane fuel cells (AEMFCs), as the next generation of cost-effective fuel cells, have attracted significant interest for more than a decade. The main advantage of the AEMFC technology is to overcome the cost of polymer electrolyte membrane fuel cells (PEMFCs) [1]. The alkaline environment allows the use of low-cost metal hardware and the design of less-expensive and non-platinum group metal (non-PGM)-based electrocatalysts. The main challenge in AEMFC is the slow kinetics of the hydrogen oxidation reaction (HOR). In alkaline media, the overall HOR process is represented as follows:

$$H_2 + 2OH^- \rightarrow 2H_2O + 2e^- \tag{7.1}$$

Three elementary steps are involved in the HOR mechanism:

1. Chemical dissociative adsorption of H_2 without electron transfer leads to two adsorbed H species (2H*). This reaction is called the Tafel reaction:

$$H_2 + 2^* \rightleftharpoons 2^*H_{ad} \tag{7.2}$$

2. Electrochemical dissociative adsorption of H_2 molecules resulting in the formation of an adsorbed hydrogen on the electrode surface is called the Heyrovsky step:

$$H_2 + * + OH^- \rightleftharpoons * - H_{ad} + e^- + H_2O \tag{7.3}$$

3. Adsorbed hydrogen atom combining with an OH^- leading to the formation of water and one electron is called the Volmer step:

$$* - H_{ad} + OH^- \leftrightharpoons * + H_2O + e^- \tag{7.4}$$

Electrocatalysis for Membrane Fuel Cells: Methods, Modeling, and Applications, First Edition.
Edited by Nicolas Alonso-Vante and Vito Di Noto.

The symbol, "*" refers to the catalytic site needed for the binding of H_2 at the electrode surface.

Due to the involvement of OH^- in the Heyrovsky and Volmer steps, fundamental understanding of the HOR pathway in alkaline media is an issue of considerable debate. The opinions can be classified into two categories, HOR pathway with OH^- in the solution [1–6] and HOR pathway with OH_{ad} on the surface of the electrocatalysts (formed by OH^- and $OH_{ad} + e^-$) [1, 7–9].

In this chapter, we focus on the hydrogen oxidation reaction in alkaline conditions. One of the main efforts is to fulfill the potential of AEMFC by designing electrocatalysts with high performance, durability, and stability. Understanding the HOR mechanism, d-band character, size, morphology, alloying, and surface modification allows us to design the next-generation electrocatalysts for HOR [10].

7.2 Mechanism of the HOR in Alkaline Media

Strmcnik et al. [7] pioneered the fundamental HOR studies and proposed that the HOR kinetics, in an alkaline medium, is limited by the Volmer step $M - H_{ads} + OH^- \Rightarrow M + H_2O + e^-$. Reactive hydroxy species (OH_{ads}) is required to promote this step. A three-dimensional volcano plot was proposed wherein the HOR rate is codetermined by the binding of the hydrogen intermediate (H_{ads}) as well as of the OH_{ads} to the surface [11]. Zhao et al. [12] used first-principles calculations for understanding the mechanism of HOR on PtNi alloy catalysts. The enhanced HOR activity of platinum in alkaline by decorating it with nickel was studied to gain more insights into the HOR mechanism, $Pt_3Ni(111)$, $Pt_2Ni_2(111)$, and $PtNi_3(111)$, and its surface alloy $PtNi_{surf}(111)$ first-principles calculations were conducted. Free energy profiles suggested that the HOR on PtNi alloys proceeds through the **Tafel–Volmer mechanism** wherein gaseous H_2 is dissociatively adsorbed on the catalyst surface to yield two adsorbed H species (Tafel reaction), followed by its reaction with OH^- in the electrolyte (the rate-determining step) to form H_2O (Volmer reaction) [13]. The HOR activity of PtNi alloy catalyst is exclusively influenced by the adsorption of hydrogen rather than hydroxyl species, even though the oxophilic behavior of platinum is enhanced by alloying with nickel. The optimal catalytic active site for HOR should possess a moderate H adsorption free energy (ΔG_{H^*}) of ~0.414 eV at a pH value of 13.

Alloying platinum with nickel elevated the d-band center (ε_d) from −2.61 to −2.08 eV, Figure 7.1, resulting in a ΔG_{H^*} value close to 0.414 eV. As a result, the free energy barrier (E_a) for the rate-determining Volmer reaction (adsorbed H* reacting with OH^- of the electrolyte) lowered and leads to the highest HOR activity observed on the bulk alloy catalytic site of $PtNi_3(111)$. The corresponding values indicative of the HOR activity, namely HOR rate (k), current density (i_0), and transfer coefficient (α), are $9.42 \times 10^3\ s^{-1}$ per site, $1.42\ mA\ cm^{-2}$, and 0.07, respectively. These results provide theoretical guidance for designing electrocatalysts with improved activity for HOR in alkaline medium.

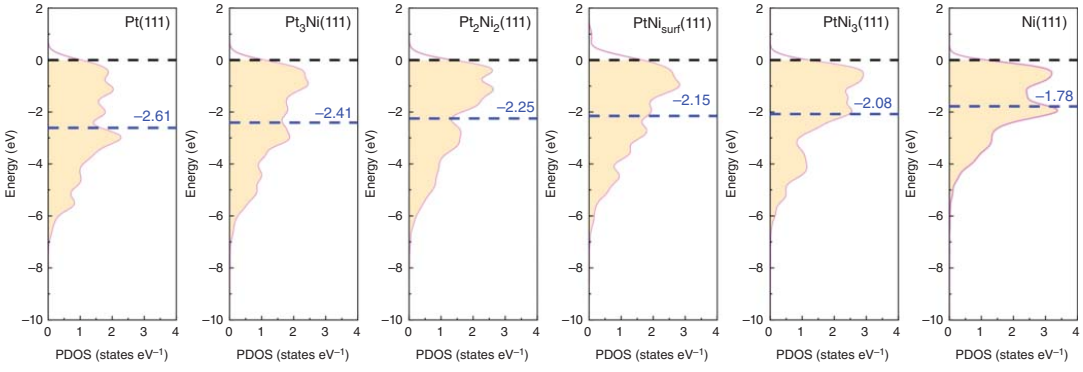

Figure 7.1 Projected density of states for the d-band of metal atoms around the FCC site for platinum, nickel, and PtNi alloys. The Fermi level marked with black dashed lines is set as the energy zero. Blue dashed lines show the d-band centers (in eV). The shadows indicate the integrating interval from the minimum energy to the Fermi level. Source: Reproduced from Ref. [12] with permission of the American Chemical Society.

In the alkaline environment, strongly oxophilic nickel will be oxidized and dissolve in the electrolyte medium as $Ni(OH)_2$. To understand the antioxidant capacity of PtNi alloys, the oxidation potential ($P_{oxidation}$) of nickel on the surface in pure Ni and PtNi alloys were calculated. The oxidation potential of nickel for Ni(111), $PtNi_3$(111), Pt_2Ni_2(111), $PtNi_{surf}$(111), and Pt_3Ni(111) were found to be 1.47, 1.05, 0.92, 0.81, and 0.74 V *vs.* SHE, respectively. The corresponding values relative to RHE were 0.70, 0.28, 0.16, 0.04, and −0.02 V, respectively, at a pH value of 13. With increasing platinum content, the oxidation potential decreases, and the corresponding antioxidant capacity increases for PtNi alloys. This is a result of the transfer of electrons from nickel to platinum in the alloys. Compared to pure nickel, the nickel atoms in the PtNi alloys have a reduced ability to provide electrons to oxygen-containing species, as some electrons on nickel are transferred to platinum. As a result, alloying nickel with platinum improves the antioxidant capacity of nickel.

Zhao et al. [12] proposed the HOR mechanism on the PtNi alloy catalyst, selected as a prototype of the highly active Pt-transition metal catalysts, for HOR in an alkaline medium at pH 13. pH 13 was chosen for modeling studies based on the experimental conditions (0.1 M KOH). The mechanism proposed is based on the first-principles DFT study yielding full free energy profiles with all the reaction barriers, hydrogen adsorption free energy, microkinetic model, and Tafel plot. The linear synchronous transition/quadratic synchronous transit method was used to locate the elementary reaction pathways and transition state (TS) and was further authenticated by the frequency calculations. Face-centered cubic close-packed (111) surface was modeled as this place possessed the lowest surface energy and is also the most abundant surface on most metal particles. Upon alloying platinum with nickel, some electrons transfer from nickel atoms to platinum atoms, leading to the positive charge center of nickel and the negative charge center of platinum atoms. This is due to the relative electronegativity values of platinum and nickel atoms, which are 2.28 and 1.91, respectively. Such formation of positive and negative charge centers is further revealed in the electron density-deformation maps of PtNi alloys. To understand the hydrogen adsorption activity of the metal surfaces, the d-band center (ε_d) of the surface metal atoms was calculated. The values of d-band centers (ε_d) of the metal surfaces Pt(111), Pt_3Ni(111), Pt_2Ni_2(111), $PtNi_{surf}$(111), $PtNi_3$(111), and Ni(111) were −2.61, −2.41, −2.25, −2.15, −2.08, and −1.78 eV, respectively. With an increase in the nickel content in the PtNi alloy, the d-band center shifted up toward the Fermi level that corresponds to the enhancement of adsorption activity of the metal surfaces with increasing content of nickel, Figure 7.1.

The H_2 molecule tends to horizontally adsorb on the top of the platinum in the PtNi alloy surfaces. The atop platinum on the PtNi alloy surface provides a stable adsorption site for H_2 while the H_2O species preferentially adsorb on the top of the nickel site. Adsorption of H_2 on atop platinum sites is regarded as physisorption as revealed from the weak adsorption energy (−0.19 to −0.37 eV) and by the elongation of bond in hydrogen in the adsorbed state (0.749–0.918 Å [H_2*] *vs.* 0.748 Å [free H_2]).

By increasing the platinum content, the interaction of H_2 with the alloy further strengthened. Adsorption of hydrogen on PtNi alloy surfaces is stronger than that on pure Pt(111) with an adsorption energy of −0.45 eV but weaker than that on Ni(111) wherein the adsorption energy is −0.72 eV. The hydrogen adsorption strength is dependent on the d-band center, ε_d, of the metal surfaces by a linear relationship, namely: $E_{ads} = -2.158 \times \varepsilon_d - 3.497$, $R^2 = 0.921\,53$. Ni(111) has a d-band center at relatively high energy ($\varepsilon_d = -1.78$ eV) compared to the d-band center of Pt(111) ($\varepsilon_d = -2.61$ eV) and, as a result, contains more empty antibonding states above the Fermi level resulting in a stronger bond with H, Figure 7.1. The d-band center (ε_d) of PtNi alloy is located between Pt(111) and Ni(111) shifted toward the Fermi level with increasing nickel content. As a result, the adsorption strength of H increases in the order: $Pt(111) < Pt_3Ni(111) < Pt_2Ni_2(111) < PtNi_{surf}(111) < PtNi_3(111) < Ni(111)$. The most stable configuration of the first hydrogen adsorption is at the fcc site on the PtNi alloy surface. The most stable adsorption site for the second hydrogen is on a similar fcc site adjacent to the first adsorbed hydrogen. The second hydrogen is adsorbed at the fcc (NiNiNi) on the $PtNi_3(111)$ surface. The adsorption energy of the second hydrogen is almost equal to the adsorption energy of the first hydrogen. The adsorption of the first hydrogen will have only a negligible effect on the adsorption of the second hydrogen atom. Even the defective surfaces, namely def-$PtNi_3(111)$, prefer to adsorb H_2O and H_2 on the top nickel and platinum atoms, respectively.

At the anode in electrolyte membrane fuel cells, the activation of water leads to the formation of various surface intermediates, which are described as different surface phases. Different surface phases, namely hydrogen-covered surface, oxygen-covered surface, hydroxyl-covered surface, and water-covered surface, on different PtNi alloy surfaces were considered. The most stable surface phase in an aqueous environment can be described by the phase diagram depicting the change in free energy (ΔG^{water}) as a function of the electrode potential (E), as shown in Figure 7.2.

The free energy changes of the reactions that connect different surface phase Equations (7.5)–(7.7) were calculated using Eq. (7.8). The free energy change values (ΔG^{water}) were plotted as a function of the whole electrode potential (E) in the phase diagrams shown in Figure 7.2.

$$H_2O\,(\text{liquid}) + * \leftrightharpoons OH^* + e^- + H^+ \tag{7.5}$$

$$OH^* + * \rightleftharpoons O^* + e^- + H^+ \tag{7.6}$$

$$* + e^- + H^+ \rightleftharpoons H^* \tag{7.7}$$

$$\Delta G = \Delta E + \Delta ZPE - T\Delta S + \Delta G_E + \Delta G_{pH} \tag{7.8}$$

The change of free energy from the initial states (ISs) to final states (FSs) used for plotting the free-energy diagrams of the HOR is calculated from Eq. (7.8) wherein ΔE is the change in energy, and ΔZPE is the change in the zero-point energy. Zero-point energies and entropies were obtained from vibrational frequency computation at $T = 298$ K. ΔS is the change in entropy from the initial and final states. ΔG_E is the

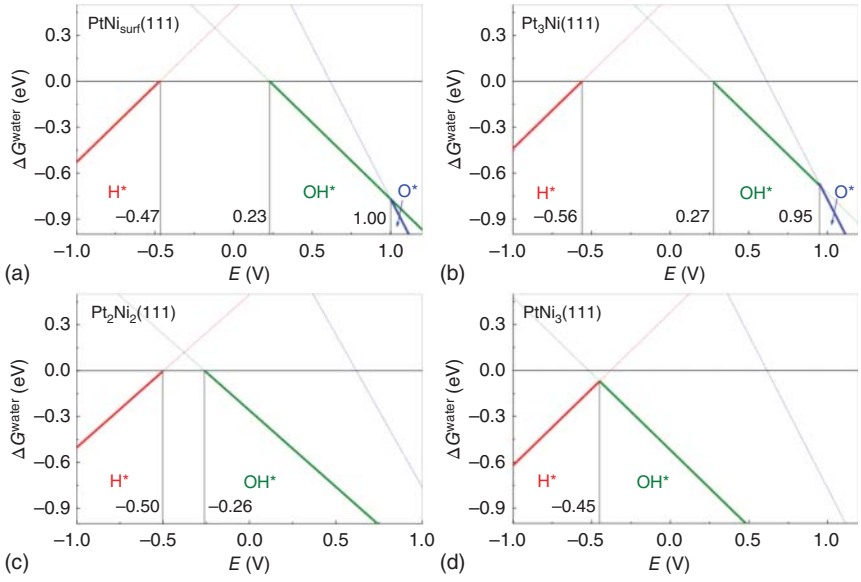

Figure 7.2 Phase diagram showing the free energy change for water in contact with different surfaces, (a) $PtNi_{surf}(111)$, (b) $Pt_3Ni(111)$, (c) $Pt_2Ni_2(111)$, and (d) $PtNi_3(111)$, as a function of whole electrode potential E. The free energy for liquid water at 298 K is defined as $\Delta G = 0$. $\Delta G_{H^*}^{Water}(E) = \Delta G_{H^*}^{Water}(0) + eE$; $\Delta G_{OH^*}^{Water}(E) = \Delta G_{OH^*}^{Water} - eE$; $\Delta G_{O^*}^{Water}(E) = \Delta G_{O^*}^{Water}(0) - 2eE$. Source: Reproduced from Ref. [12] with permission of the American Chemical Society.

bias effect on the free energy of the states involving an electron in the electrode $\Delta G_E = -neE$, where n is the number of the transferred electrons (e), and E is the whole electrode potential including the polarization effect (*vs.* SHE). U is set to be 0.059 V (*vs.* SHE), and ΔG_{pH} is the correction for the free energy of the H^+ ion at $pH \neq 0$. $\Delta G_{pH} = k_b T \cdot \ln 10 \cdot pH$, where k_b is the Boltzmann constant and pH = 13. In the phase diagram, Figure 7.2 shows the change in the free energy of water in contact with different surfaces as a function of whole electrode potential E, at 298 K and at a pH of 13. The lowest line corresponds to the thermodynamically most stable phase. The crossings of two bottom lines represent a phase change. At very negative potential, only hydrogen is stably adsorbed on all alloyed surfaces. Likewise, the surfaces of the alloy catalyst are covered with oxygen at high positive potentials. Upon alloying platinum with nickel, the potential of $H_2O^* \rightarrow OH^*$ phase transition is shifted downward (toward lower potential values), resulting in a reduction in the H_2O phase with an increase in the OH* phase as the nickel content in the alloy is increased. On $PtNi_3(111)$ surface, the clean surface disappears completely, and a transition from H* to OH* phase is observed at −0.45 and −0.46 V, respectively, and this is due to the increase in the oxophilic behavior of NiPt alloys with increasing nickel content since nickel is more oxophilic than platinum. This observation is further supported by the order of the OH adsorption energies of −0.10, −0.21, −0.25, −0.75, −1.01, and −1.14 eV on Pt(111), $Pt_3Ni(111)$, $PtNi_{surface}(111)$, $Pt_2Ni_2(111)$, $PtNi_3(111)$, and Ni(111) surfaces, respectively.

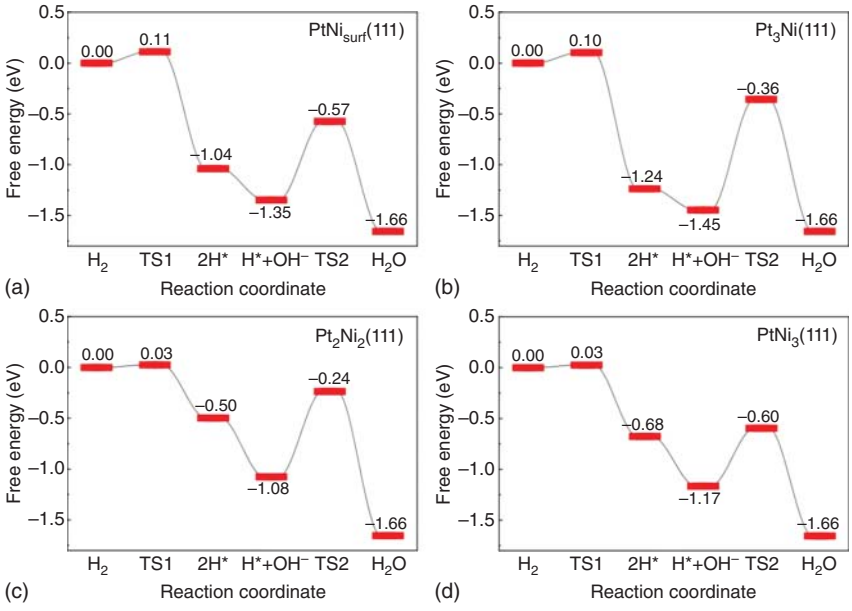

Figure 7.3 Free energy diagram of Tafel–Volmer mechanism involved in the HOR on (a) PtNi$_{surf}$(111), (b) Pt$_3$Ni(111), (c) Pt$_2$Ni$_2$(111), and (d) PtNi$_3$(111) at pH 13 and $T = 298$ K. Source: Reproduced from Ref. [12] with permission of the American Chemical Society.

For the alkaline HOR all possible elementary reactions were studied on PtNi$_{surf}$(111), Pt$_3$Ni(111), Pt$_2$Ni$_2$(111), and PtNi$_3$(111), and the calculated activation energy barriers of the reactions and the corresponding free energy changes as a function of reaction coordinate are depicted in Figure 7.3. Among the five possible elementary reactions of HOR, the Tafel reaction involving the dissociative adsorption of H_2 offers a low-energy pathway with an activation barrier in the range of 0.12–0.26 eV. On the contrary, for the Heyrovsky reactions, the H_2 reacts with either OH^- in solution or with adsorbed OH; the activation energy barrier is high in the range of 0.54–1.56 eV on all the PtNi alloy surfaces studied. The activation energy barrier for the subsequent Volmer reaction involving oxidative desorption of H* forming H_2O, Eq. (7.5), is 0.70–1.18 eV; the activation barrier is lower than that of the recombination of adsorbed OH and H, Eq. (7.6), 1.06–1.77 eV. However, the activation barrier for the Volmer reaction is still higher than that of Tafel reaction. Therefore, HOR on PtNi alloy surfaces prefers the Tafel–Volmer mechanism, with the Volmer reaction being the rate-determining step. The free energy diagrams, which represent the elementary processes of the most favorable Tafel–Volmer pathway on PtNi$_{surface}$(111), Pt$_3$Ni(111), Pt$_2$Ni$_2$(111), and PtNi$_3$(111), are shown in Figure 7.3. From the plots of free energy over the reaction coordinate, the activation energy barrier for the rate-determining reaction, i.e. oxidative desorption of H* to H_2O through the transitions state (TS2), is the lowest (−0.60 eV) on the surface of PtNi$_3$(111) compared to any other PtNi alloy as the ideal catalyst with higher HOR activity. The optimal H adsorption free energy change for HOR (ΔG_{H^*}) is

0.414 eV. The free-energy change, for the whole HOR (ΔG_{HOR}), was calculated to be −1.656 eV. $PtNi_3(111)$ exhibited the highest HOR activity with the lowest free energy barrier E_a, the smallest value of $|\Delta G_{H^*} - 0.414|$, the highest rate constant, and the largest exchange current density.

To enhance the HOR activity of an electrocatalyst in an alkaline medium, it is essential to identify the alkaline HOR pathway and the rate-determining step.

7.3 Electrocatalysts for Alkaline HOR

In alkaline electrolytes, the HOR activity of the pure platinum-group metal (PGM) catalysts (Pt, Ir, and Pd) is significantly reduced by at least two orders of magnitude compared to the same PGMs under acidic conditions [2, 3, 14, 15]. In this regard, the development of electrocatalysts with comparable or much higher activity for alkaline HOR is the key to the overall performance enhancement of AEMFC. In this section, the recent development in PGM-based and non-PGM alkaline HOR electrocatalysts will be discussed.

7.3.1 Platinum Group Metal HOR Electrocatalysts

The activity of the catalysts for HOR depends on a combination of several parameters, such as the support, the morphology of electroactive catalyst species, composition, and size. The implementation of those parameters in the design of the electrocatalysts is crucial for achieving synergistic catalyst activity leading to enhanced overall fuel cell performance. Recently, the insertion of heteroatom into carbon has been used to improve the interaction between the nanoparticles and the support. For example, Kundu et al. [16] studied the effect of nitrogen-doped carbon as a support for Pt nanoparticles. In this study, they showed that the metallic platinum domains offered adsorption sites for the hydrogen atom; PtO_x promoted the adsorption of OH-species; and the N-doped carbon support acted as the highly conductive matrix favoring the charge transfer process. The presence of nitrogen, in the carbon matrix, leads to an improvement in the interaction between the hydrogen atoms and the catalyst surface. Bhowmik et al. [17] examined the interaction between palladium and carbon-nitride nanosheets, which led to improved activity, compared to commercial Pd/C, and attributed this phenomenon to the synergic effect between palladium nanoparticles and the support. Much research was also placed in using CeO_2 as support. The introduction of CeO_2 to palladium resulted in a fivefold increase in the performance and a 20-fold increase in the specific and mass activity compared to Pd/C [18]. The Pd—H bond interactions were weakened in the presence of CeO_2. The oxophilic nature of CeO_2 supplies reactive OH species that would remove the H_{ads} intermediate for the surface of palladium, resulting in improved HOR kinetics [18, 19]. The addition of 3d transition metal, such as

nickel, leads to an enhancement of activity. For example, the Pd/Ni nanocomposite, which was synthesized by reducing the palladium complex on the nickel surface, in an aqueous solution, leads to the enhancement of HOR activity [8]. While evaluating the performance in a membrane electrode assembly for alkaline fuel cells a peak of 400 mW cm^{-2} was obtained, which is more than twice as much as that of a pure palladium catalyst. The high activity is attributed to the presence of OH_{ads} species on the surface of the oxophilic nickel that favor HOR kinetics. Since the distribution of palladium and nickel leads to the enhancement in HOR performance, three designed core–shell nanoparticulated catalysts of Pd@Ni, Ni@Pd, and NiPd alloys were tested as electrocatalysts for HOR [20]. The highest activity was measured on NiPd-alloyed nanoparticles and was attributed to the synergistic electrocatalytic effect between nickel and palladium surface atoms. Another example to enhance palladium activity is by decorating tungsten with palladium (Pd-d-W). The Pd-d-W electrocatalysts were designed by activating the surface of tungsten with palladium ions using a galvanic displacement reaction. The interaction between palladium and the oxophilic surface of tungsten oxide enhances the activity of palladium, leading to a reduction in the onset potential and an increase in specific current density. The effect on the enhanced HOR activity is attributed to the adsorption of the OH species near the surface of the palladium atoms [21]. Previous studies demonstrated that alloying is an effective way to enhance the HOR activity. For example, Pt–Ru alloy nanoparticles were found to improve drastically the HOR activity and the cell performance to about twice compared to platinum nanoparticle electrocatalysts [22]. Besides, Ru–Ir alloy nanoparticles increased the HOR activity to about four times compared to individual Ru, Ir, and Pt nanoparticle-based electrocatalysts [23]. Small metal nanoparticles of Ru–Ir (3.7 nm) supported on carbon were designed and tested to investigate the effect of alloying on the HOR activity. The Ru–Ir pair was found to be 19.5 and 3.5 times higher than the Ru–Ru and Ir–Ir pairs, respectively. The Tafel slope analysis suggested that the Ru–Ir pair promoted the Volmer step through the bifunctional mechanism. Ruthenium and iridium offer reactive OH^- and H species, resulting in an accelerated reaction between these species and thereby enhancing the HOR activity. Mao et al. [24] synthesized atomically dispersed nickel on ruthenium (Ni/Ru) which showed better HOR activity than bimetallic RuNi, pristine Ru, and commercial Pt/C catalysts. Isolation of nickel atoms on ruthenium nanocrystals optimized the hydrogen binding energy and decreased the free energy of the formation of water. The weakening of hydrogen binding energy, high electrochemically active surface area, and suitable oxophilic behavior are achieved by alloying platinum with ruthenium and supporting the alloy nanoparticles (3.0–3.8 nm) of $Pt_{0.25}Ru_{0.75}$ on nitrogen-doped carbon. The mass-specific activity of $Pt_{0.25}Ru_{0.75}$/N-doped carbon electrocatalyst was 1654 A g^{-1}(PtRu), and this value is 4.7 and 4 times higher than the activity of Pt/C and PtRu/C catalysts [25]. Mass activity superior to that of PtRu/C catalysts was achieved by confining the atomic clusters of ruthenium in the TiO_2 lattice. The electrocatalysts are CO tolerant and

exhibited high HOR activity up to a potential of 0.9 V *vs.* RHE. Selective HOR is observed even with high CO content (10 vol%). Abundant Ru—Ti bond formations were observed along the TiO_2 lattice. Efficient electron transfer from electron-rich TiO_2 to Ru is attributed to the selective HOR and improved CO tolerance [26]. Alloying ruthenium with a 3d transition metal such as cobalt leads to a shift in the d-band and a weakening of H adsorption on ruthenium. Among RuCo, RuNi, and RuFe alloys, catalyst $Ru_{0.95}Co_{0.05}/C$ synthesized by impregnation method exhibited best HOR and ORR activities [27]. HOR activity of Pt/C modified with nickel was enhanced by the immersion of Pt/C in nickel chloride solution, leading to a weakening in the hydrogen adsorption. The specific mass current density was increased by 18% from 23.8 to 33.4 A g^{-1}. Modification of platinum with oxophilic metals was proposed as a way to improve the anodic electrocatalysts for HOR [28].

Table 7.1 summarizes the current state-of-the-art PGM-based HOR catalysts. As can be seen, different strategies were applied to enhance HOR activity and control the kinetics of the reaction. Such approaches are controlling the size, tuning the morphology, alloying with two or three metals, and improving the interaction between the metal and support. The main drawback is the use of precious metal. The idea of reducing them or not using them at all is needed and should further be explored by applying nonprecious metal electrocatalysts as a primary catalytic center.

7.3.2 Non-platinum Group Metal-based HOR Electrocatalysts

Compared to PEMFCs, the main advantage of AEMFCs is the fact that nonprecious metals offer good performance and could replace the use of platinum group metal as anode electrocatalysts [44–46]. H_2 is a chemically reactive gas, which adsorbs on most transition metal surfaces [47]. Among all those transition metals, nickel attracted much more attention but, unfortunately, has not been successful being used as a sole component for alkaline HOR electrocatalyst until now. Therefore, many efforts were implemented to enhance the alkaline HOR activity of nickel-based electrocatalysts to replace precious metals. Nickel nanoparticles supported on N-doped carbon nanotubes (Ni/N-CNT) have been synthesized by a wet chemical method [48]. When comparing the activity with pure nickel nanoparticles, Ni/N-CNT leads to a 21-fold increase in activity and is attributed to the synergetic effect between N-CNT and nickel. To further enhance the HOR activity, nickel-based catalysts supported on carbon matrices doped with diverse nonmetallic elements such as B, S, and N were investigated [49]. Those hybrid catalysts were designed using two steps: pyrolysis and reduction and compared to Ni/C. The activity order is as follows: Ni/SC > Ni/NC > Ni/BC ~ Ni/C, where SC, NC, and BC correspond to the S-, N-, and B-doped carbon support materials. Two main factors were proposed to improve activity: (i) the anchoring effect leading to smaller and more uniform particle sizes with large ECSA and (ii) the metal–support interaction that weakens the hydrogen bonding energy of nickel, leading to better specific activity [49]. To correlate the observed HOR activity of

Table 7.1 Summary of PGM-based electrocatalysts for alkaline HOR.

Electrocatalyst	Electrolyte concentration (M)/T (°C)	Mass activity @$\eta = 50$ mV (mA $mg^{-1}_{catalyst}$)	j_0 ECSA normalized (mA $cm^{-2}_{catalyst}$)	References
Pt/Au polycrystalline	0.1 M KOH/—	—	$1.580_{geometric}$	[29]
Pt/Au/C	0.1 M KOH/—	—	$2.750_{geometric}$	[29]
5% Pt/Vulcan XC72	0.1 M NaOH/40 °C	2052.00	1.710	[3]
10% Pd/Vulcan XC72	0.1 M NaOH/40 °C	115.50	0.110	[3]
10% Ir/Vulcan XC72	0.1 M NaOH/40 °C	448.40	0.760	[3]
Pt/C	1.0 M KOH/—	79.00	0.590	[30]
PdIr/C	1.0 M KOH/—	138.00	1.700	[30]
Pd/Au $\theta_{Pd}/Au = 0.39$	0.1 M NaOH/20 °C	—	1.700	[31]
Pd/Au $\theta_{Pd}/Au = 0.23$	0.1 M NaOH/20 °C	—	4.000	[31]
Pt/Cu nanowires	0.1 M KOH/—	330.00	1.010	[32]
20% Ir/C	0.1 M KOH/20 °C	292.30	0.470	[33]
20% Ir/C-300 °C	0.1 M KOH/20 °C	284.60	0.540	[33]
20% Ir/C-500 °C	0.1 M KOH/20 °C	260.40	0.620	[33]
20% Ir/C-600 °C	0.1 M KOH/20 °C	307.20	0.960	[33]
20% Ir/C-800 °C	0.1 M KOH/20 °C	187.70	1.360	[33]
1.5% Pd/Ni	0.1 M KOH	—	0.570	[34]
Ir_{NS}	0.1 M NaOH/25 °C	—	0.810	[35]
5% Pt/C	0.1 M KOH/20 °C	659.00	1.030	[4]
10% Pd/C	0.1 M KOH/20 °C	72.30	0.090	[4]
20% Ir/C	0.1 M KOH/20 °C	313.00	0.490	[4]
20% Rh/C	0.1 M KOH/20 °C	690.00	0.860	[4]
Pt nanowire	0.1 M KOH/—	99.00	$1.380_{geometric}$	[36]
PtRu nanowire	0.1 M KOH/—	157.00	$2.200_{geometric}$	[36]

(Continued)

Table 7.1 (Continued)

Electrocatalyst	Electrolyte concentration (M)/T (°C)	Mass activity @$\eta = 50$ mV (mA $mg^{-1}_{catalyst}$)	j_0 ECSA normalized (mA $cm^{-2}_{catalyst}$)	References
PtFe nanowire	0.1 M KOH/—	120.00	$1.680_{geometric}$	[36]
PtCo nanowire	0.1 M KOH/—	117.00	$1.640_{geometric}$	[36]
PtCu nanowire	0.1 M KOH/—	69.00	$0.970_{geometric}$	[36]
PtAu nanowire	0.1 M KOH/—	88.00	$1.23_{geometric}$	[36]
$PdNi_{NP}$	0.1 M KOH/—	3.90	$0.197_{geometric}$	[8]
Pd-CN_X	0.5 M KOH/—	—	$0.080_{geometric}$	[17]
20% Pd/C	0.1 M KOH/20 °C	91.90	0.120	[37]
20% Pd/C-300C	0.1 M KOH/20 °C	92.30	0.140	[37]
20% Pd/C-400C	0.1 M KOH/20 °C	76.20	0.230	[37]
20% Pd/C-500C	0.1 M KOH/20 °C	44.20	0.260	[37]
20% Pd/C-600C	0.1 M KOH/20 °C	17.10	0.240	[37]
Ir/CeO_2–C	0.1 M KOH/20 °C	73.5	$0.092_{geomtric}$	[38]
Pd-Ni/C	0.1 M KOH/—	104.00 ($\eta = 100$ mV)	1.380 ($\eta = 100$ mV)	[20]
Pt/C	0.1 M KOH/25 °C	403.00	0.226	[39]
IrNi/C	0.1 M KOH/25 °C	188.00	0.214	[39]
IrNi@PdIr/C	0.1 M KOH/25 °C	854.00	0.209	[39]
Ir_2Ru_1NWs/C	0.1 M KOH/—	994.00	0.099	[40]
Ir_1Ru_1NWs/C	0.1 M KOH/—	1416.00	0.126	[40]
Ir_1Ru_2NWs/C	0.1 M KOH/—	1813.00	0.0932	[40]
Ir_1Ru_3NWs/C	0.1 M KOH/—	3346.00	0.084	[40]
BCC PdCu/C-500 °C	0.1 M KOH/R.T.	522.00	$0.883_{geomtric}$	[41]
PtRu/C	0.1 M KOH/R.T.	1023.00	$1.463_{geomtric}$	[41]
IrNi@Ir	0.1 M KOH/R.T.	1.12	1.220 ± 0.100	[42]
$RuNi_1$	0.1 M KOH/R.T.	270.00	—	[24]
Pt/C	0.1 M KOH/R.T.	426.00	—	[24]
$IrMo_{0.59}$ nanoparticles	0.1 M KOH/30 °C	3850.00	1.150	[43]
Ir nanoparticles	0.1 M KOH/30 °C	690.00	0.320	[43]

ECSA, electrochemical surface area; j_0, exchange current density; θ_{Pd}, the palladium coverage; NW, nanowires.

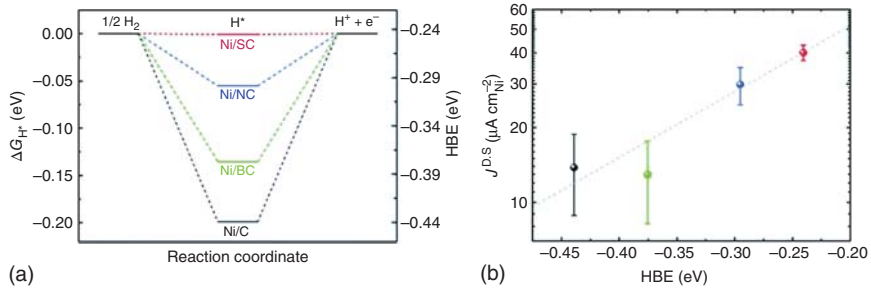

Figure 7.4 (a) Calculated adsorption free energy of H, ΔG_{H^*}, and HBE; (b) Dependence of exchange current density on the relative hydrogen binding energies (HBE). Source: Reproduced from Ref. [49] with permission of the Royal Society of Chemistry.

nickel supported on heteroatom-doped carbon supports to their Gibbs adsorption free energies of H (ΔG_{H^*}) or hydrogen binding energies (HBEs), density functional theory calculations were carried out. The values of Gibbs adsorption free energies of H, $|\Delta G_{H^*}|$, followed the order, Ni/SC < Ni/NC < Ni/BC < Ni/C, as shown in Figure 7.4a. The catalyst Ni/SC exhibited an optimal value of (~0 eV) Gibbs adsorption free energy of H (ΔG_{H^*}). As predicted theoretically from the DFT studies, Ni/SC exhibited 2.9 and 7.7 times higher specific activity and mass activity, respectively, than the dopant-free Ni/C catalyst. A linear relationship between the specific activity and the hydrogen binding energies of the four different catalysts studied, Ni/SC, Ni/NC, Ni/BC, and Ni/C, is observed, Figure 7.4b. The enhanced activity in the nickel-supported heteroatom-doped carbon supports, especially Ni/SC, is attributed to the strong metal–support interaction leading to enhance an HOR activity [49].

Another interesting catalyst is Ni_3N supported on carbon (Ni_3N/C) designed by reducing the nickel precursor under NH_3 atmosphere at elevated temperature [50]. Ni_3N/C presented the highest mass activity for HOR and breakdown potential for a PGM-free catalyst. The activity was attributed to the nickel d-band center downshifts and interfacial charge transfer from Ni_3N to the carbon support as factors leading to the weak binding of hydrogen and oxygen species in Ni_3N/C. The weak binding of hydrogen was suggested as the main reason for the high HOR activity. Bifunctional HOR mechanism, namely the dissociative adsorption of H and recombination of adsorbed intermediate species H* and OH* to form water, is not possible on pure nickel. This is due to the strong adsorption of hydrogen and a high activation barrier for the recombination reaction. The relatively strong adsorption of H (H_{ad}) is the main reason for the slow HOR kinetics on pure nickel. On the contrary, in the bimetallic NiCu catalyst with as low as 5% Cu, nearly 50% surface coverage of copper is observed, and therefore, weakening of (H_{ad}) hydrogen adsorption energy as well as decrease in the activation energy barrier for the recombination of H_{ad} and OH_{ad} was observed. Compared to nickel electrocatalyst, 10-fold enhancement in the Volmer step was achieved [51]. Wang et al. [52] prepared Ni–Cu binary alloy films by combinatorial magnetron co-sputtering method. A Volcano-type relationship was observed between HOR activity and copper content in the Ni–Cu bimetallic alloy

film. With Ni–Cu binary alloy film containing 40 at.% Cu, the exchange current density was four times higher than that of pure nickel. Interfacial engineering resulted in a unique Ni_3N/Ni electrocatalyst which exhibits excellent HOR and HER activity [53]. The active sites are located at the interface of Ni_3N and nickel supported on Ni-foam. The electrocatalyst showed zero overpotential, long-term durability, 100% Faradaic efficiency, and excellent CO tolerance. The free-energy change for the adsorption of hydrogen at the interfacial sites was found to be almost zero. In the presence of CO, the maximum current density of Ni_3N/Ni/Nickel-foam decreased from 6.95 to 6.71 mA cm^{-2} (only 3.5% decrease). Another work that uses the strategy to construct the surface between metals and metal nitrides as an effective approach to design electrocatalysts for HOR is from Song et al. [54]. Low-cost Co_2N/Co electrocatalysts are designed through a facile electrodeposition and nitridation approach. The DFT calculation reveals the significant role of Co_2N/Co interfacial sites that possessed optimal hydrogen adsorption energy as well as facilitated water adsorption and dissociation on the catalyst surface. The electrocatalyst exhibited CO tolerance and long-term stability for HOR. Yang et al. [55] synthesized CeO_2-decorated nickel hybrid nanoparticles supported on carbon black (Vulcan XC-72) using solvothermal synthesis (CeO_2(r)-Ni/C-1). DFT calculations revealed that the improved HOR performance is associated with the promoted OH* adsorption energy and optimal ΔG_{H^*} obtained from the synergistic effect between oxygen vacancy contained in CeO_2 and nickel species. The oxygen vacancies at the surface of the CeO_2 played an important role in accelerating the HOR kinetics in alkaline media.

The required demand for low-cost and earth-abundant electrocatalysts for the HOR led to the development of electrocatalysts using metal–organic frameworks (MOF). Yang et al. [56] designed Ni/NiO/C electrocatalyst protected by graphene using direct annealing of nickel-based MOF (Ni-BTC) and showed nearly zero onset potential, strong robustness, and great tolerance toward CO poisoning. Computational, electrochemical studies together with physical characterization show that the interfacing of Ni and NiO in Ni/NiO/C, with the presence of highly conductive graphene layers, leads to optimal binding energies of hydrogen and hydroxide species contributing to the overall HOR activity. Ni et al. [57] annealed $Ni_3(BTC)_2$ under nitrogen and low concentration of hydrogen (0, 1, 2, and 4 vol%), yielding carbon-supported nickel nanoparticles with the highest activity for HOR reported so far using non-PGM-based electrocatalysts.

Table 7.2 summarizes the non-PGM electrocatalysts designed in the past few years for HOR in alkaline conditions. As can be seen, the most common nickel-based catalysts take advantage of the oxophilic feature of Ni to tune their electronic properties. While adjusting the size, morphology, and composite with other transition metals and supports, it is possible to modulate the Ni activity and stability toward the best performing and low-cost electrocatalysts for HOR.

Table 7.2 Summary of non-PGM-based electrocatalysts for HOR.

Electrocatalyst	Electrolyte concentration (M)/T (°C)	Mass activity @η = 50 mV (mA $mg^{-1}_{catalyst}$)	j_0 ECSA normalized (mA $cm^{-2}_{catalyst}$)	References
CoNiMo	0.1 M KOH/20 °C	—	0.0150	[58]
$Ni_{0.95}Cu_{0.05}$/C	0.1 M NaOH/25 °C	1.5	0.0140	[29]
$Ni_{0.95}Cu_{0.05}$/Vulcan XC-72	0.1 M KOH/25 °C	2.5	0.0140	[59]
Ni/N-CNT	0.1 M KOH/R.T.	9.3	0.0280	[48]
Ni/CNT	0.1 M KOH/R.T.	1.9	0.0092	[48]
Ni	0.1 M KOH/R.T.	0.28	0.0013	[48]
Ni_3@h-$(BN)_1$/C-700NH_3	0.1 M KOH/—	—	0.0220	[60]
NiMo/KB	0.1 M NaOH/25 °C	4.5	0.0270	[61]
$Ni_{95}Cu_5$/KB	0.1 M KOH/—	—	0.0250	[62]
Ni/Ni_3N/NF	0.1 M KOH/25 °C	—	0.0030	[53]
Nonactivated Ni_{ED}/XC-72	0.1 M NaOH/25 °C	—	0.0062	[63]
Ch-activated NiED/XC72[a)]	0.1 M NaOH/25 °C	—	0.0560	[63]
EC-activated NiED/XC72[a)]	0.1 M NaOH/25 °C	—	0.0390	[63]
CeO_2(r)-Ni/C-1	0.1 M KOH/30 °C	12.28	0.0380	[64]
CeO_2-Ni/C-1	0.1 M KOH/30 °C	8.48	0.0260	[64]
Ni/C	0.1 M KOH/30 °C	5.89	0.0160	[64]
Ni/SC	0.1 M KOH/30 °C	11.0	0.0402	[49]
Ni/NC	0.1 M KOH/30 °C	—	0.0309	[49]
Ni/BC	0.1 M KOH/30 °C	—	0.0130	[49]
Ni/C	0.1 M KOH/30 °C	—	0.0148	[49]
Ni_3N/C	0.1 M KOH/—	24.38	0.0140	[49]
Ni_3N	0.1 M KOH/—	1.73	0.0170	[49]
Ni-Ref	0.1 M KOH/—	1.07	0.0020	[49]
Ni/NiO/C-700	0.1 M KOH/—	5.0	0.0260	[56]
Ni	0.1 M KOH/R.T.	—	0.0140	[65]
WNi_4	0.1 M KOH/R.T.	—	0.0680	[65]
$MoNi_4$	0.1 M KOH/R.T.	—	0.0650	[65]
Ni-H_2-2%	0.1 M KOH/—	50.4	0.028	[57]

j_0, exchange current density; CNT, carbon nanotube; h-BN, hexagonal boron nitride; KB, Ketjen black; ECSA, electrochemical surface area.

a) Nanostructured Ni nanoparticles supported on Vulcan XC-72 carbon (NiED/XC-72); The electrode subjected to oxidation either under contact with air (Ch activated) or by applying positive potential (EC activated); Reduction of Ni precursors via $NaBH_4$ in the presence of CeO_2 and XC-72 (CeO_2(r)-Ni/C-1); Heteroatoms-doped carbon supports (XC, X = S, N, or B).

7.4 Conclusions

This chapter provides fundamental information on the state-of-the-art PGM and non-PGM-based electrocatalysts for the HOR in alkaline conditions. One of the main challenges in the commercialization of AEMFCs is the slow kinetics of the HOR reaction, especially in the alkaline medium with PGM-based electrocatalysts compared to the acidic medium. The solution to overcome this problem depends on developing nickel-based systems with an emphasis on the downward shift of the d-band center of Ni(111) (−1.78 eV) away from the Fermi level. Strategies for shifting downward the d-band center (ε_d) of nickel were discussed (in the specific examples of $PtNi_3$(111) and Ni_3N systems). Such a strategy is crucial as the hydrogen adsorption strength varies linearly with the d-band center of the metal surfaces. Further, there exists a linear relationship between the hydrogen binding energies of the anode electrocatalyst and HOR specific activity. HOR reaction on Pt Ni alloys suggested proceeding through the Tafel–Volmer mechanism involving the dissociative adsorption of gaseous hydrogen on the catalyst surface yielding two adsorbed hydrogen species (Tafel reaction) and the subsequent reaction of adsorbed hydrogen with OH^- in the electrolyte to form H_2O (Volmer reaction, the rate-determining step). The optimal H adsorption free energy for HOR (ΔG_{H^*}) and the free energy change for the whole HOR (ΔG_{HOR}) with the ideal HOR anode electrocatalyst $PtNi_3$ were found to be 0.414 and −1.656 eV. By a downward shift of the d-band center of nickel in the Ni_3N system, optimal hydrogen binding is achieved, resulting in a remarkable HOR activity (mass activity, 24.38 mA mg^{-1} catalyst). Another strategy for achieving the best HOR performance from nickel nanoparticles, via weakening of their hydrogen binding energy, is through a strong metal–support interaction. In a specific example, sulfur-doped carbon material support facilitated strong metal (Ni)–support interaction and has significantly weakened the hydrogen binding energy, leading to high HOR activity (mass activity, 11.0 mA mg^{-1} catalyst). Adopting a similar strategy of tuning the metal–support interaction to impose strain on the active catalytic sites (nickel nanoparticles in constrained geometry), Hu's group succeeded in designing the state-of-the-art anode electrocatalyst for HOR with outstanding activity (mass activity@η = 50 mV, 50.4 mA mg^{-1} catalyst) [57]. The nickel nanoparticle active sites in constrained geometries are achieved by choosing a peculiar Ni-metal–organic framework precursor and pyrolyzing the precursor in an N_2–H_2 (2 vol%) environment, leading to the formation of polycrystalline nickel nanoparticles (6.5 ± 2.9 nm). Charge transfer phenomenon from a nickel to carbon support was attributed to the downward shifting of the nickel d-band center away from the Fermi level, resulting in lower binding energies of H_{ads} and OH_{ads}. Overall, shifting the d-band center of nickel downward from the Fermi level leading to lowering of hydrogen binding energy appears to be the key to the success in finding the best nonnoble metal Ni-based anode electrocatalyst for HOR. This can be achieved by tuning the metal–support interaction and imposing strain on the geometry and configuration of nickel active sites. Such geometric and electronic effects between the active species (nickel nanoparticles) and extensively heteroatom-functionalized carbon supports (oxygen/sulfur/nitrogen) resulting

from novel catalyst synthesis strategies are the path ahead to the groundbreaking invention in this field of research. The key parameters to be optimized are the location of the d-band center and the hydrogen binding energy of nickel nanoparticles in the Ni/C systems. This leaves much scope for the synthetic, electrochemical, and theoretical chemists to work on designing strategies for the nanoarchitecture of Ni/C systems for future anode electrocatalysts for HOR.

Acronyms

AEMFC	alkaline electrolyte membrane fuel cell
CNT	carbon nanotubes
DFT	density functional theory
ECSA	electrochemical surface area
FSs	final states
HBE	hydrogen energy binding
HOR	hydrogen oxidation reaction
ISs	initial states
MOF	metal-organic frameworks
N-CNT	N-doped carbon nanotube
PEMFC	polymer electrolyte membrane fuel cell
PGM	platinum group metal
RHE	reversible hydrogen electrode
SHE	standard hydrogen electrode
TS	transition state

References

1 Campos-Roldán, C.A. and Alonso-Vante, N. (2019). The hydrogen oxidation reaction in alkaline medium: an overview. *Electrochemical Energy Reviews* 2 (2): 312–331.

2 Sheng, W., Gasteiger, H.A., and Shao-Horn, Y. (2010). Hydrogen oxidation and evolution reaction kinetics on platinum: acid vs alkaline electrolytes. *Journal of the Electrochemical Society* 157 (11): B1529.

3 Durst, J., Siebel, A., Simon, C. et al. (2014). New insights into the electrochemical hydrogen oxidation and evolution reaction mechanism. *Energy & Environmental Science* 7 (7): 2255–2260.

4 Zheng, J., Sheng, W., Zhuang, Z. et al. (2016). Universal dependence of hydrogen oxidation and evolution reaction activity of platinum-group metals on pH and hydrogen binding energy. *Science Advances* 2 (3): 1–9.

5 Elbert, K., Hu, J., Ma, Z. et al. (2015). Elucidating hydrogen oxidation/evolution kinetics in base and acid by enhanced activities at the optimized Pt shell thickness on the Ru core. *ACS Catalysis* 5 (11): 6764–6772.

6 Rheinländer, P.J., Herranz, J., Durst, J., and Gasteiger, H.A. (2014). Kinetics of the hydrogen oxidation/evolution reaction on polycrystalline platinum in alkaline electrolyte reaction order with respect to hydrogen pressure. *Journal of the Electrochemical Society* 161 (14): F1448–F1457.

7 Strmcnik, D., Uchimura, M., Wang, C. et al. (2013). Improving the hydrogen oxidation reaction rate by promotion of hydroxyl adsorption. *Nature Chemistry* 5 (4): 300–306.

8 Alesker, M., Page, M., Shviro, M. et al. (2016). Palladium/nickel bifunctional electrocatalyst for hydrogen oxidation reaction in alkaline membrane fuel cell. *Journal of Power Sources* 304: 332–339.

9 Alia, S.M., Pivovar, B.S., and Yan, Y. (2013). Platinum-coated copper nanowires with high activity for hydrogen oxidation reaction in base. *Journal of the American Chemical Society* 135 (36): 13473–13478.

10 Ishikawa, K., Ohyama, J., Okubo, K. et al. (2020). Enhancement of alkaline hydrogen oxidation reaction of Ru-Ir alloy nanoparticles through bifunctional mechanism on Ru-Ir pair site. *ACS Applied Materials & Interfaces* 12 (20): 22771–22777.

11 Koper, M.T.M. (2013). Hydrogen electrocatalysis: a basic solution. *Nature Chemistry* 5 (4): 255–256.

12 Zhao, L., Liu, H., Liu, Y. et al. (2020). Mechanistic insights into the hydrogen oxidation reaction on PtNi alloys in alkaline media: a first-principles investigation. *ACS Applied Materials & Interfaces* 12 (36): 40248–40260.

13 Campos-Roldán, C.A., Calvillo, L., Granozzi, G., and Alonso-Vante, N. (2020). Alkaline hydrogen electrode and oxygen reduction reaction on Pt_xNi nanoalloys. *Journal of Electroanalytical Chemistry* 857: 113449.

14 Markovic, N.M., Gasteiger, H.A., and Ross, P.N. (1995). Oxygen reduction on platinum low-index single-crystal surfaces in sulfuric acid solution. Rotating ring – Pt(hkl) disk studies. *Journal of Physical Chemistry* 99 (11): 3411–3415.

15 Rheinländer, P., Henning, S., Herranz, J., and Gasteiger, H.A. (2013). Comparing hydrogen oxidation and evolution reaction kinetics on polycrystalline platinum in 0.1 M and 1 M KOH. *ECS Transactions* 50 (2): 2163–2174.

16 Kundu, M.K., Bhowmik, T., Mishra, R., and Barman, S. (2018). Platinum nanostructure/nitrogen-doped carbon hybrid: enhancing its base media HER/HOR activity through bi-functionality of the catalyst. *ChemSusChem* 11 (14): 2388–2401.

17 Bhowmik, T., Kundu, M.K., and Barman, S. (2016). Palladium nanoparticle-graphitic carbon nitride porous synergistic catalyst for hydrogen evolution/oxidation reactions over a broad range of pH and correlation of its catalytic activity with measured hydrogen binding energy. *ACS Catalysis* 6 (3): 1929–1941.

18 Miller, H.A., Lavacchi, A., Vizza, F. et al. (2016). A Pd/C-CeO_2 anode catalyst for high-performance platinum-free anion exchange membrane fuel cells. *Angewandte Chemie International Edition* 55 (20): 6004–6007.

19 Miller, H.A., Vizza, F., Marelli, M. et al. (2017). Highly active nanostructured palladium-ceria electrocatalysts for the hydrogen oxidation reaction in alkaline medium. *Nano Energy* 33: 293–305.

20 Shviro, M., Polani, S., Dunin-Borkowski, R.E., and Zitoun, D. (2018). Bifunctional electrocatalysis on Pd-Ni core–shell nanoparticles for hydrogen oxidation reaction in alkaline medium. *Advanced Materials Interfaces* 5 (9): 1–8.

21 Arulrajan, A.C., Subramanian, P., Singh, R.K., and Schechter, A. (2020). Pd-decorated tungsten as Pt-free bimetallic catalysts for hydrogen oxidation reaction in alkaline electrolyte. *Israel Journal of Chemistry* 60 (5–6): 563–569.

22 Wang, Y., Wang, G., Li, G. et al. (2015). Pt-Ru catalyzed hydrogen oxidation in alkaline media: oxophilic effect or electronic effect? *Energy & Environmental Science* 8 (1): 177–181.

23 Ohyama, J., Kumada, D., and Satsuma, A. (2016). Improved hydrogen oxidation reaction under alkaline conditions by ruthenium-iridium alloyed nanoparticles. *Journal of Materials Chemistry A* 4 (41): 15980–15985.

24 Mao, J., He, C.T., Pei, J. et al. (2020). Isolated Ni atoms dispersed on Ru nanosheets: high-performance electrocatalysts toward hydrogen oxidation reaction. *Nano Letters* 20 (5): 3442–3448.

25 Cong, Y., Chai, C., Zhao, X. et al. (2020). $Pt_{0.25}Ru_{0.75}$/N-C as highly active and durable electrocatalysts toward alkaline hydrogen oxidation reaction. *Advanced Materials Interfaces* 7 (11): 1–9.

26 Zhou, Y., Xie, Z., Jiang, J. et al. (2020). Lattice-confined Ru clusters with high CO tolerance and activity for the hydrogen oxidation reaction. *Nature Catalysis* 3 (5): 454–462.

27 Wang, H., Yang, Y., Disalvo, F.J., and Abrunã, H.D. (2020). Multifunctional electrocatalysts: Ru-M (M = Co, Ni, Fe) for alkaline fuel cells and electrolyzers. *ACS Catalysis* 10 (8): 4608–4616.

28 Huang, X., Long, C., Han, J. et al. (2020). Remarkably enhanced hydrogen oxidation reaction activity of carbon-supported Pt by facile nickel modification. *Chemical Research in Chinese Universities* 36 (1): 105–109.

29 Mahoney, E.G., Sheng, W., Yan, Y., and Chen, J.G. (2014). Platinum-modified gold electrocatalysts for the hydrogen oxidation reaction in alkaline electrolytes. *ChemElectroChem* 1 (12): 2058–2063.

30 Jervis, R., Mansor, N., Gibbs, C. et al. (2014). Hydrogen oxidation on PdIr/C catalysts in alkaline media. *Journal of the Electrochemical Society* 161 (4): F458–F463.

31 Henning, S., Herranz, J., and Gasteiger, H.A. (2015). Bulk-palladium and palladium-on-gold electrocatalysts for the oxidation of hydrogen in alkaline electrolyte. *Journal of the Electrochemical Society* 162 (1): F178–F189.

32 Alia, S.M. and Yan, Y. (2015). Palladium coated copper nanowires as a hydrogen oxidation electrocatalyst in base. *Journal of the Electrochemical Society* 162 (8): F849–F853.

33 Zheng, J., Zhuang, Z., Xu, B., and Yan, Y. (2015). Correlating hydrogen oxidation/evolution reaction activity with the minority weak hydrogen-binding sites on Ir/C catalysts. *ACS Catalysis* 5 (7): 4449–4455.

34 Bakos, I., Paszternák, A., and Zitoun, D. (2015). Pd/Ni synergestic activity for hydrogen oxidation reaction in alkaline conditions. *Electrochimica Acta* 176: 1074–1082.

35 Montero, M.A., De Chialvo, M.R.G., and Chialvo, A.C. (2016). Evaluation of the kinetic parameters of the hydrogen oxidation reaction on nanostructured iridium electrodes in alkaline solution. *Journal of Electroanalytical Chemistry* 767: 153–159.

36 Scofield, M.E., Zhou, Y., Yue, S. et al. (2016). Role of chemical composition in the enhanced catalytic activity of Pt-based alloyed ultrathin nanowires for the hydrogen oxidation reaction under alkaline conditions. *ACS Catalysis* 6 (6): 3895–3908.

37 Zheng, J., Zhou, S., Gu, S. et al. (2016). Size-dependent hydrogen oxidation and evolution activities on supported palladium nanoparticles in acid and base. *Journal of the Electrochemical Society* 163 (6): F499–F506.

38 Qin, B., Yu, H., Chi, J. et al. (2017). A novel Ir/CeO_2-C nanoparticle electrocatalyst for the hydrogen oxidation reaction of alkaline anion exchange membrane fuel cells. *RSC Advances* 7 (50): 31574–31581.

39 Qin, B., Yu, H., Jia, J. et al. (2018). A novel IrNi@PdIr/C core-shell electrocatalyst with enhanced activity and durability for the hydrogen oxidation reaction in alkaline anion exchange membrane fuel cells. *Nanoscale* 10 (10): 4872–4881.

40 Qin, B., Yu, H., Gao, X. et al. (2018). Ultrathin IrRu nanowire networks with high performance and durability for the hydrogen oxidation reaction in alkaline anion exchange membrane fuel cells. *Journal of Materials Chemistry A* 6 (41): 20374–20382.

41 Qiu, Y., Xin, L., Li, Y. et al. (2018). BCC-phased PdCu alloy as a highly active electrocatalyst for hydrogen oxidation in alkaline electrolytes. *Journal of the American Chemical Society* 140 (48): 16580–16588.

42 Liu, D., Lu, S., Xue, Y. et al. (2019). One-pot synthesis of IrNi@Ir core-shell nanoparticles as highly active hydrogen oxidation reaction electrocatalyst in alkaline electrolyte. *Nano Energy* 59 (January): 26–32.

43 Fu, L., Li, Y., Yao, N. et al. (2020). IrMo nanocatalysts for efficient alkaline hydrogen electrocatalysis. *ACS Catalysis* 10 (13): 7322–7327.

44 Cong, Y., Yi, B., and Song, Y. (2018). Hydrogen oxidation reaction in alkaline media: from mechanism to recent electrocatalysts. *Nano Energy* 44: 288–303.

45 Campos-Roldán, C.A., Calvillo, L., Boaro, M. et al. (2020). NiO-Ni/CNT as an efficient hydrogen electrode catalyst for a unitized regenerative alkaline microfluidic cell. *ACS Applied Energy Materials* 3 (5): 4746–4755.

46 Li, Y., Li, Z., Cong, H. et al. (2022). Boosting hydrogen oxidation performance of phase-engineered Ni electrocatalyst under alkaline media. *ACS Sustainable Chemistry & Engineering* 10 (11): 3682–3689.

47 Davydova, E.S., Mukerjee, S., Jaouen, F., and Dekel, D.R. (2018). Electrocatalysts for hydrogen oxidation reaction in alkaline electrolytes. *ACS Catalysis* 8 (7): 6665–6690.

48 Zhuang, Z., Giles, S.A., Zheng, J. et al. (2016). Nickel supported on nitrogen-doped carbon nanotubes as hydrogen oxidation reaction catalyst in alkaline electrolyte. *Nature Communications* 7: 1–8.

49 Yang, F., Bao, X., Zhao, Y. et al. (2019). Enhanced HOR catalytic activity of PGM-free catalysts in alkaline media: the electronic effect induced by different heteroatom doped carbon supports. *Journal of Materials Chemistry A* 7 (18): 10936–10941.

50 Ni, W., Krammer, A., Hsu, C.S. et al. (2019). Ni_3N as an active hydrogen oxidation reaction catalyst in alkaline medium. *Angewandte Chemie International Edition* 58 (22): 7445–7449.

51 Salmazo, D., Juarez, M.F., Oshchepkov, A.G. et al. (2019). On the feasibility of bifunctional hydrogen oxidation on Ni and NiCu surfaces. *Electrochimica Acta* 305: 452–458.

52 Wang, G., Li, W., Huang, B. et al. (2019). Exploring the composition-activity relation of Ni-Cu binary alloy electrocatalysts for hydrogen oxidation reaction in alkaline media. *ACS Applied Energy Materials* 2 (5): 3160–3165.

53 Song, F., Li, W., Yang, J. et al. (2018). Interfacing nickel nitride and nickel boosts both electrocatalytic hydrogen evolution and oxidation reactions. *Nature Communications* 9 (1): 4531.

54 Song, F., Li, W., Yang, J. et al. (2019). Interfacial sites between cobalt nitride and cobalt act as bifunctional catalysts for hydrogen electrochemistry. *ACS Energy Letters* 4 (7): 1594–1601.

55 Yang, F., Bao, X., Li, P. et al. (2019). Boosting hydrogen oxidation activity of Ni in alkaline media through oxygen-vacancy-rich CeO_2/Ni heterostructures. *Angewandte Chemie International Edition* 58 (40): 14179–14183.

56 Yang, Y., Sun, X., Han, G. et al. (2019). Enhanced electrocatalytic hydrogen oxidation on Ni/NiO/C derived from a nickel-based metal–organic framework. *Angewandte Chemie International Edition* 58 (31): 10644–10649.

57 Ni, W., Wang, T., Schouwink, P.A. et al. (2020). Efficient hydrogen oxidation catalyzed by strain-engineered nickel nanoparticles. *Angewandte Chemie* 132 (27): 10889–10893.

58 Sheng, W., Bivens, A.P., Myint, M. et al. (2014). Non-precious metal electrocatalysts with high activity for hydrogen oxidation reaction in alkaline electrolytes. *Energy & Environmental Science* 7 (5): 1719–1724.

59 Cherstiouk, O.V., Simonov, P.A., Oshchepkov, A.G. et al. (2016). Electrocatalysis of the hydrogen oxidation reaction on carbon-supported bimetallic NiCu particles prepared by an improved wet chemical synthesis. *Journal of Electroanalytical Chemistry* 783: 146–151.

60 Gao, L., Wang, Y., Li, H. et al. (2017). A nickel nanocatalyst within a h-BN shell for enhanced hydrogen oxidation reactions. *Chemical Science* 8 (8): 5728–5734.

61 Kabir, S., Lemire, K., Artyushkova, K. et al. (2017). Platinum group metal-free NiMo hydrogen oxidation catalysts: high performance and durability in alkaline exchange membrane fuel cells. *Journal of Materials Chemistry A* 5 (46): 24433–24443.

62 Roy, A., Talarposhti, M.R., Normile, S.J. et al. (2018). Nickel-copper supported on a carbon black hydrogen oxidation catalyst integrated into an anion-exchange membrane fuel cell. *Sustainable Energy & Fuels* 2 (10): 2268–2275.

63 Oshchepkov, A.G., Bonnefont, A., Pronkin, S.N. et al. (2018). Nanostructured nickel nanoparticles supported on vulcan carbon as a highly active catalyst for the hydrogen oxidation reaction in alkaline media. *Journal of Power Sources* 402 (September): 447–452.

64 Yang, F., Bao, X., Li, P. et al. (2019). Boosting hydrogen oxidation activity of Ni in alkaline media through oxygen-vacancy-rich CeO_2/Ni heterostructures. *Angewandte Chemie* 131 (40): 14317–14321.

65 Duan, Y., Yu, Z.Y., Yang, L. et al. (2020). Bimetallic nickel-molybdenum/tungsten nanoalloys for high-efficiency hydrogen oxidation catalysis in alkaline electrolytes. *Nature Communications* 11 (1): 1–10.